THE ASTROPHYSICAL JOURNAL, 493:715–729, 1998 February 1
© 1998. The American Astronomical Society. All rights reserved. Printed in U.S.A.

PROGRESS ON ESTABLISHING THE SPATIAL DISTRIBUTION OF MATERIAL RESPONSIBLE FOR THE $\frac{1}{4}$ keV SOFT X-RAY DIFFUSE BACKGROUND LOCAL AND HALO COMPONENTS

S. L. SNOWDEN,[1,2,3] R. EGGER,[1] D. P. FINKBEINER,[4,5] M. J. FREYBERG,[1] AND P. P. PLUCINSKY[6]

Received 1997 February 14; accepted 1997 September 8

ABSTRACT

In this paper we present a new look at the distribution of emission responsible for the soft X-ray diffuse background (SXRB) using *ROSAT* all-sky survey data. This is prompted by the demonstration of the existence of extensive $\frac{1}{4}$ keV emission in the Galactic halo that was not considered in the most successful previous model, in which the bulk of the observed $\frac{1}{4}$ keV X-rays originated in a Local Hot Bubble (LHB) that surrounds the Sun. The basic distribution can be represented by two angularly varying Galactic components (the LHB and an X-ray halo) and an isotropic extragalactic component. In addition, there are the distinct enhancements of supernova remnants, superbubbles, and clusters of galaxies.

Using the negative correlation between the SXRB and *DIRBE*-corrected *IRAS* 100 μm intensity, we find a LHB that is similar to previous models, although it is possibly more limited in extent. The emission of the LHB varies by a factor of ~ 3.3 with direction and produces *ROSAT* $\frac{1}{4}$ keV intensities between ~ 250 and $\sim 820 \times 10^{-6}$ counts s^{-1} arcmin^{-2} (typically brighter at higher Galactic latitudes), with inferred emission measures of ~ 0.0018 to 0.0058 cm^{-6} pc (assuming thermal ionization equilibrium). The distribution of the emission temperature of the LHB is peaked at $10^{6.07}$ K with a range of $\pm 12\%$ at FWHM. While this variation is small and is perhaps due to systematic uncertainties in the analysis, there is a suggestion of a cooler region in the anticenter direction consistent with previous studies.

We derive halo plus extragalactic intensities that vary from ~ 400 to $\gtrsim 3000 \times 10^{-6}$ counts s^{-1} arcmin^{-2} outside the absorbing gas of the Galactic disk. As the low end of the range is comparable to what is expected for the extragalactic background, this implies that the halo emission varies considerably over the sky, with inferred emission measures ranging from near zero to > 0.02 cm^{-6} pc. The distribution of emission temperatures in the halo, again derived from thermal equilibrium emission models, peaks near $10^{6.02}$ K and varies over $\pm 20\%$ at FWHM.

Subject headings: diffuse radiation — Galaxy: halo — X-rays: galaxies — X-rays: ISM

1. INTRODUCTION

The source of the $\frac{1}{4}$ keV soft X-ray diffuse background (SXRB) has proved elusive since its discovery in the late 1960s (Bowyer, Field, & Mack 1968; Henry et al. 1968; Bunner et al. 1969). The general negative correlation between the $\frac{1}{4}$ keV background and the column density of Galactic neutral hydrogen (dominated by a Galactic plane-to-pole variation) was strongly suggestive of an "absorption" model, in which the angular structure of the SXRB is produced by the absorption of a flux of distant origin (e.g., Bowyer et al. 1968; Marshall & Clark 1984). The absence of the expected detailed negative correlation (some specific H I features showed little indication of shadowing; Burrows et al. 1984), the shallowness of the apparent absorption (the fitted effective cross sections for absorption were significantly smaller than model values), and the weakness of the energy dependence of the apparent absorption (McCammon et al. 1983) encouraged the investigation of other possibilities. Principal among these were the "interspersed" and "displacement" models. The interspersed model (Jakobsen & Kahn 1986; Kahn & Jakobsen 1988; Hirth et al. 1992) suggested that the X-ray–emitting and X-ray–absorbing material are extensively intermixed as in the McKee & Ostriker (1977) model of the interstellar medium, which has a large filling factor of hot plasma with embedded clouds of cooler neutral material. The general negative correlation between the two could be explained with appropriate scale heights and midplane densities, while the requirement for detailed negative correlation would be relaxed. With clumping of the absorbing material to the extent that the individual clumps become optically thick at $\frac{1}{4}$ keV, the weakness and energy independence of the absorption could also be explained. However, some of the requirements of the interspersed model were in disagreement with observations, most notably with constraints on clumping of the absorbing gas (Burrows 1989; Burrows & Kraft 1993).

By the end of the 1980s, the displacement model (Sanders et al. 1977; Snowden et al. 1990, hereafter SCMS) proved to be the most consistent with the available data. The displacement model suggests that the irregularly shaped cavity that surrounds the Sun (known independently from interstellar absorption-line studies: Frisch & York 1983; Paresce 1984;

[1] Max-Planck-Institut für Extraterrestrische Physik, D-85740 Garching, Germany.
[2] Code 662, NASA/Goddard Space Flight Center, Greenbelt, MD 20771.
[3] Universities Space Research Association.
[4] Department of Astronomy, 601 Campbell Hall, University of California, Berkeley, Berkeley, CA 94720-3411.
[5] NSF Graduate Fellow.
[6] Harvard-Smithsonian Center for Astrophysics, 60 Garden Street, Cambridge, MA 02138.

Welsh et al. 1994, and N_H studies: Knapp 1975) contains an X-ray–emitting plasma, and that the cavity is extended more toward the Galactic poles than within the Galactic plane. The greater the extent of the plasma-filled cavity in a given direction, the greater the emission measure of the plasma and the lower the measured column density of H I (at least at constant Galactic latitude), which produces the general negative correlation between the two. The displacement model provided a natural explanation for the weakness and energy independence of the apparent absorption and allowed for H I features that had no apparent effect on the X-ray flux. See McCammon & Sanders (1990) for a review of our knowledge of the $\frac{1}{4}$ keV SXRB circa 1990.

The displacement model was an admittedly simplistic approach to modeling the true distribution of emission. In addition to emission from the Local Hot Bubble (LHB; Cox & Reynolds 1987; the region of hot plasma surrounding the Sun), there are several other obvious contributors to the SXRB. Several supernova remnants and superbubbles provide obvious and extensive emission in the $\frac{1}{4}$ keV band, and the clearly extragalactic flux observed at higher energies ($\gtrsim 1$ keV) is expected to contribute at least small amounts to the observed $\frac{1}{4}$ keV flux as well. However, the supposition that the *bulk* of the observed flux originated within the LHB was rather successful (SCMS).

With the launch of the *Röntgensatellit* (*ROSAT*; Trümper 1983, 1992), the situation became more complicated. One of the first unique discoveries of *ROSAT* was the observation of deep shadows in the general SXRB cast by the Draco Nebula ($l, b \sim 90°, 40°$; Burrows & Mendenhall 1991; Snowden et al. 1991). These observations unequivocally proved that there is significant $\frac{1}{4}$ keV X-ray emission in at least the lower Galactic halo: roughly 50% of the *observed* flux in that direction originates $\gtrsim 300$ pc from the Sun, $\gtrsim 200$ pc above the Galactic plane. Additional studies using both pointed observations (e.g., Wang & Yu 1995) and all-sky survey data (e.g., Snowden et al. 1994a; Herbstmeier et al. 1995) demonstrated that the shadows were not unique to Draco but were common features of the $\frac{1}{4}$ keV SXRB. Recent studies using the data from multiple *ROSAT* pointings (e.g., Juda 1996; Sidher et al. 1996) have addressed to a limited extent the issue of the variations of the local and distant emission.

Using the high-resolution *ROSAT* all-sky survey maps (Snowden et al. 1997) and *DIRBE*-corrected *IRAS* 100 μm intensities (Schlegel, Finkbeiner, & Davis 1998; hereafter SFD), we reexamine the displacement model for the observed $\frac{1}{4}$ keV SXRB. The observed flux is modeled as emission from an unabsorbed local component, an absorbed Galactic halo component, and an absorbed isotropic extragalactic component. The Galactic components are not fixed to any specific geometric form, but the local component is assumed (and forced) to be smooth over scales of 5°–10°. The analysis is insensitive to any structure on finer scales. We find that while X-ray emission in the LHB is similar to that discussed in SCMS, the contribution from Galactic halo and extragalactic emission provides up to $\sim$ one-half of the observed intensity in some directions and $\sim$one-fourth of the *observed* photons over the entire sky. After correcting for Galactic interstellar absorption, the derived halo emission measures can be near zero or as much as several times larger than those within the LHB, although they are typically comparable to the brighter LHB regions.

2. DATA

2.1. *X-Ray Data*

In this paper we use the R1 and R2 band data (PSPC PI channels 8–19 and 20–41, respectively; defined in Snowden et al. 1994b and with band response functions displayed in Fig. 1) from the *ROSAT* all-sky survey (Snowden & Schmitt 1990; Voges 1992) as presented in Snowden et al. (1997). An extensive discussion of the data and the details of the data reduction can be found in Snowden et al. (1994b, 1995b, 1997) and references therein. While the data are available in $12' \times 12'$ pixels, they are binned in $24' \times 24'$ pixels for our analysis to improve the individual statistics.

The *ROSAT* survey data have been cleaned of noncosmic background contamination and have been corrected for variations of exposure, vignetting, and detector artifacts. In addition, they have point sources removed to 0.025 counts s^{-1} in the R1 + R2 (or $\frac{1}{4}$ keV) band, a uniform threshold over $\sim$90% of the sky. One source at the threshold in a $24' \times 24'$ pixel will increase the intensity of that pixel by $\sim$15% of the *minimum* surface brightness on the sky. The density of such sources on the sky (within a factor of 2 of the threshold) is <1 deg^{-2}, or one for every $\sim$10 pixels. This implies that unresolved discrete sources may increase the scatter in our fits but not significantly affect results.

Figure 2 shows the distribution of the statistical significance (I/σ_I, measured intensity I divided by the uncertainty in the measured intensity σ_I) of the $24' \times 24'$ pixels. Typical values are between $\sim$4 and $\sim$10 with some dependence on the band. The units used in this paper for the X-ray intensity are detector specific and are typically 10^{-6} counts s^{-1} arcmin^{-2}. While the conversion between observed intensity and flux is spectral model–dependent, an unabsorbed 10^6 K thermal equilibrium emission model (Raymond & Smith 1977) will produce $\sim 10 \times 10^{-6}$ counts s^{-1} arcmin^{-2} from a flux of 1 keV cm^{-2} s^{-1} sr^{-1} keV^{-1} at 0.2 keV.

2.2. *Measures of Galactic Absorption*

Maps of the 21 cm H I emission line have traditionally been used to estimate the amount of X-ray–absorbing

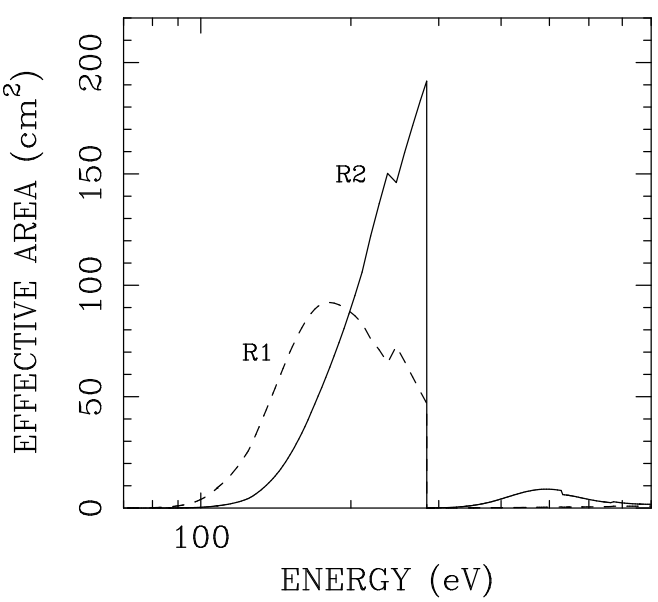

FIG. 1.—On-axis band response curves for the *ROSAT* R1 and R2 bands. The sharp break at 0.284 keV is due to the carbon Kα absorption edge of the PSPC entrance window.

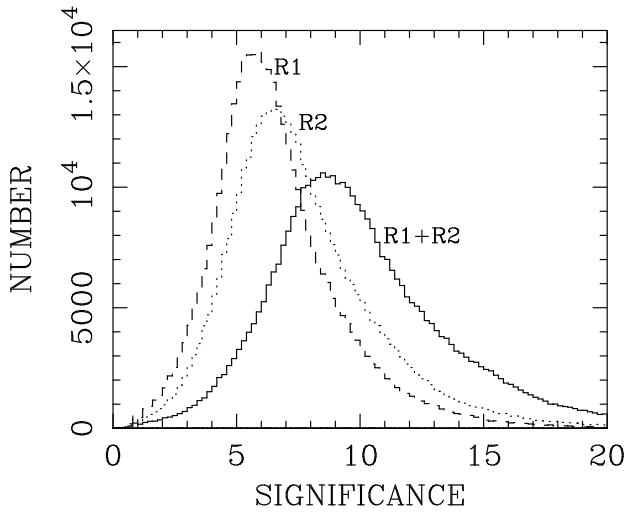

FIG. 2.—Histogram of the statistical significance (count rate divided by the uncertainty in the count rate, I/σ_I) for the 24′ × 24′ pixels for the R1 (*dashed*), R2 (*dotted*), and R1 + R2 (*solid*) bands.

material along a line of sight in the Galaxy. This can underestimate the actual absorption that is due to saturation effects or the presence of molecular gas, neither of which is too important at high latitudes, or that is due to neutral or singly ionized helium associated with ionized hydrogen (e.g., the Reynolds layer, a distribution of ionized hydrogen that has been detected in the Galactic halo; Reynolds 1991). The biggest drawback of these maps for the analysis of *ROSAT* data, however, is their poor angular resolution relative to the X-ray data (at best ∼0°.5 for surveys that cover large areas of the sky at high latitudes; e.g., 36′ for the Leiden-Dwingeloo H I survey; Hartmann & Burton 1997). On the other hand, long-wavelength infrared emission as measured by *IRAS* and *COBE* appears to correlate well with total interstellar mass, and the *IRAS* 100 μm data have an angular resolution of ∼5′, which is a good match to the *ROSAT* X-ray survey. However, the *IRAS* data have an uncertain gain at low spatial frequencies and a poorly determined zero point. Variations in the dust temperature would also be expected to affect the conversion from IR brightness to mass column density. In the maps used here, the low spatial frequencies in the *IRAS* 100 μm data have been replaced by those from the well-calibrated *DIRBE* data (SFD). The zodiacal emission of the interplanetary dust has been modeled with a simple three-parameter modulation of the *DIRBE* 25 μm map and has been eliminated. Furthermore, over 8000 point sources have been removed, and residual striping in the *IRAS* images have been filtered using a Fourier destriping algorithm. Finally, the *DIRBE* 100 μm and 240 μm data have been used to determine temperature variations and to correct the 100 μm map to a constant reference temperature, after which it is converted to an $E(B-V)$ reddening using extragalactic calibrators. The zero point of the SFD map is linked to the zero point of the Leiden-Dwingeloo 21 cm survey data (Hartmann & Burton 1997) in the velocity range from -74 km s^{-1} to 24 km s^{-1}, in low column density directions far from the Galactic plane. The quoted velocity range excludes dust-deficient high-velocity clouds (Wakker & Boulanger 1986). As with the H I data themselves, the effect of the Reynolds layer is not included. Hereafter, we will refer to the cleaned, corrected, and scaled 100 μm data as SFD data. Figure 3 shows the correlation between the SFD data and the Leiden-Dwingeloo H I data in the specified velocity range.

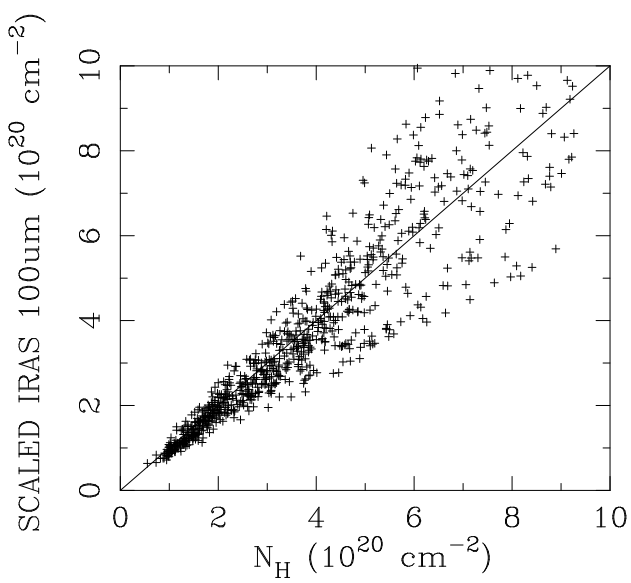

FIG. 3.—Scatter plot of the corrected and scaled *IRAS* 100 μm data vs. the data from the Leiden-Dwingeloo H I survey.

Since the SFD data provide no separation of components or distances such as those derived for H I data from velocity information, we consider only the total Galactic column density of absorbing material in a simple foreground/background slab-absorption model. Other papers (e.g., Kerp et al. 1997 with high-velocity clouds) will consider the possibility of X-ray emission interspersed between different velocity components of the H I. There is evidence in at least the Ursa Major region that the nonintermixed emission and absorption model is reasonable. In this direction there are H I clouds at both ~ -45 km s^{-1} and ~ -10 km s^{-1} that show deep shadows with equal foreground intensities implying that there is no additional emission in the path length between the two clouds (Snowden et al. 1994a). However, there is also evidence for at least one absorbing cloud of significant N_H that lies within the hot plasma of the LHB (Kerp, Herbstmeier, & Mebold 1993) near the direction of the Draco Nebula. Such clouds are of some concern for our analysis because they will lower the fitted foreground LHB contribution and raise the fitted halo contribution. So far they do not appear to be common.

3. ANALYSIS

In order to determine the foreground and distant (relative to the Galactic absorbing gas) contributions to the observed $\frac{1}{4}$ keV SXRB, we examine the negative correlation between the $\frac{1}{4}$ keV background and the column density of absorbing material along the line of sight as measured by the SFD data. To do so, we divide the sky into 4°.8 × 4°.8 regions with the 24′ × 24′ pixels. The spacing of the regions is 3°.2 × 3°.2, which provides some angular overlap. The choice of the region size and overlap is not critical to the analysis (we used several and derived similar results). The size of the region was minimized to sample as fine an angular structure as feasible and to reduce the effect of any intrinsic larger scale variation. The region could not be made smaller without losing the needed dynamic range in the absorbing column density and affecting the robustness

of the results. Having an overlap simply has the effect of smoothing the results (which are subsequently further smoothed).

The supposition is that on small angular scales no reasonable geometry will give a significant negative correlation owing to displacement of H I by X-ray–emitting gas, as clearly happens on large angular scales (SCMS). This is the critical difference between this work and previous studies. With the high angular resolution and statistical significance provided by the *ROSAT* data, the negative correlation of absorption on small angular scales can be distinguished from the presumed smoother, larger scale variations of displacement.

With the X-ray intensity and effective $N_{\rm H}$ for each $24' \times 24'$ pixel, we fitted a two-component absorption model (foreground plus absorbed halo emission) plus a fixed extragalactic contribution, which is also absorbed,

$$I_{\rm X} = I_0 + I_1 \times \exp\left[-\sigma(N_{\rm H}, T) \times N_{\rm H}\right] + I_{\rm eg} \times \exp\left[-\sigma(N_{\rm H}, \alpha) \times N_{\rm H}\right],$$

to all pixels in each $4\overset{\circ}{.}8 \times 4\overset{\circ}{.}8$ region independently for the R1 and R2 bands. $I_{\rm X}$ is the observed X-ray intensity; I_0 is the fitted foreground component; I_1 is the fitted halo component that is absorbed by the column density $N_{\rm H}$; $\sigma(N_{\rm H}, T)$ is the theoretical band-averaged absorption cross section (Morrison & McCammon 1983), which is a function both of $N_{\rm H}$ and the temperature, T, of the thermal equilibrium emission model (Raymond & Smith 1977; J. C. Raymond 1991, private communication–computer code update; Raymond 1992; see Snowden et al. 1994b); $I_{\rm eg}$ is the fixed extragalactic contribution; and $\sigma(N_{\rm H}, \alpha)$ is the theoretical band-averaged absorption cross section, which is a function both of $N_{\rm H}$ and power-law index, α.

$I_{\rm eg}$ is fixed using the results of recent observations of shadowing by extragalactic objects (a R1 + R2 band flux of $\sim 400 \times 10^{-6}$ counts s^{-1} arcmin^{-2}; e.g., M101, Snowden & Pietsch 1995; NGC 55, Barber, Roberts, & Warwick 1996a; several additional face-on galaxies, Cui et al. 1996) and the extragalactic spectrum determined by Hasinger et al. (1993), $I(E) \sim E^{-1.96}$. The unabsorbed R2/R1 band ratio of 0.96 for the power-law spectrum places 204×10^{-6} counts s^{-1} arcmin^{-2} in the R1 band and 196×10^{-6} counts s^{-1} arcmin^{-2} in the R2 band.

In this analysis we ignore absorption due to the Reynolds layer (Reynolds 1991), the distribution of H II gas above the disk of the Galaxy whose associated He I and He II can add the equivalent of $\gtrsim 0.5 \times 10^{20}$ H I cm^{-2} in absorption. We do so because the distribution and column density of the Reynolds layer remains uncertain, and, furthermore, there is no evidence to place the halo X-ray emission either in front of, or behind, this possible additional source of absorption. A column density of 0.5×10^{20} H I cm^{-2} increases the optical depth by ~ 0.4. If the halo X-ray emission originates beyond such a column, our results will underestimate the halo emission measure by $\sim 50\%$.

For a variety of reasons, the quality of the fits varies over the sky, as does the sensitivity for the determination of the foreground and distant components. Poor statistics of the X-ray data, and more fundamentally low survey exposure times, as well as any intrinsic variation of I_0 or I_1 over the region (including any residual systematic errors in the survey flux), will decrease the accuracy of the fits and will often increase the χ^2_ν values. The χ^2_ν histogram of the fits in the northern and southern polar regions is displayed in Figure 4 and peaks at about 1.3. While formally statistically unacceptable for the typical number of degrees of freedom (~ 140), the value is rather good when compared to other similar analyses (e.g., Snowden et al. 1994a). In addition, the large values arise apparently from nonstatistical scatter in the data rather than an error in the model curve. Thus, the fitted foreground values and to a lesser extent the fitted background values are relatively reliable as averages for the regions. The uncertainties in this analysis are difficult to quantify since many of the errors are systematic, but experience suggests that the foreground values are good to $\pm 25 \times 10^{-6}$ counts s^{-1} arcmin^{-2}. In order to give the "flavor" of the fits, Figure 5 shows scatter plots of the R12 band and scaled *IRAS* data along with the fitted model curves for eight representative northern hemisphere regions; their χ^2_ν values are also listed. It can be seen from the extent of the scatter and the size of the error bars that the deviations are a relatively small percent of the total flux and that the general trend of the data is well represented by the model curves.

The ability to distinguish between foreground and background emission is constrained by the dynamic range of the effective $N_{\rm H}$ over the region. For instance, regions near the Galactic plane provide no information on the distant component because the Galactic H I is completely optically thick to $\frac{1}{4}$ keV X-rays. However, the foreground component is well determined, at least away from distinct emission features. The existence of any additional emission in the region not considered by the model (e.g., if the region contains a supernova remnant [SNR] or an X-ray–bright cluster of galaxies) will increase the χ^2 statistic of the fit and will affect the fitted parameters. We have, therefore, excluded regions affected by a limited number of bright, small-scale extended sources such as the Cygnus Loop and Vela SNRs and the Virgo and Coma clusters of galaxies. Large features (e.g., $>10°$) are not removed as they are resolved in our analysis

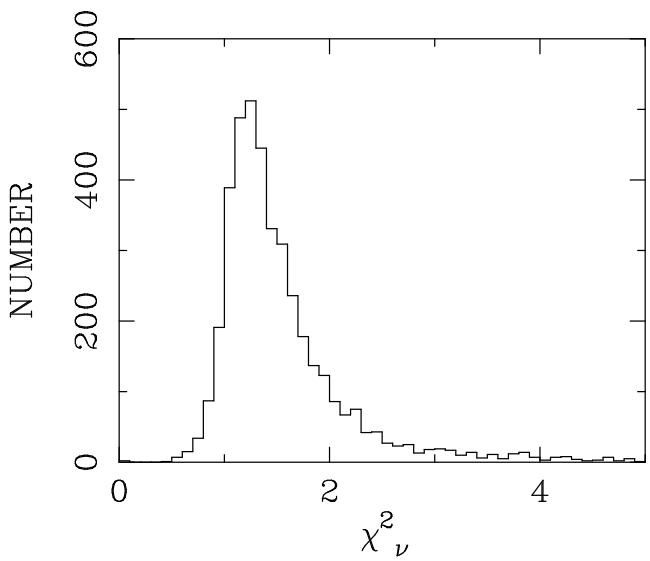

FIG. 4.—Histogram of the χ^2_ν values for the fits in the northern and southern polar regions. Note that the peak of the distribution (the northern and southern distributions were similar) is ~ 1.3, which is relatively good for fits of this type (see, e.g., Snowden et al. 1994a). However, there is a high χ^2_ν tail, which indicates that some regions were formally very poorly fitted (e.g., the Draco region, which was covered with high exposure and therefore had small errors for the individual pixels).

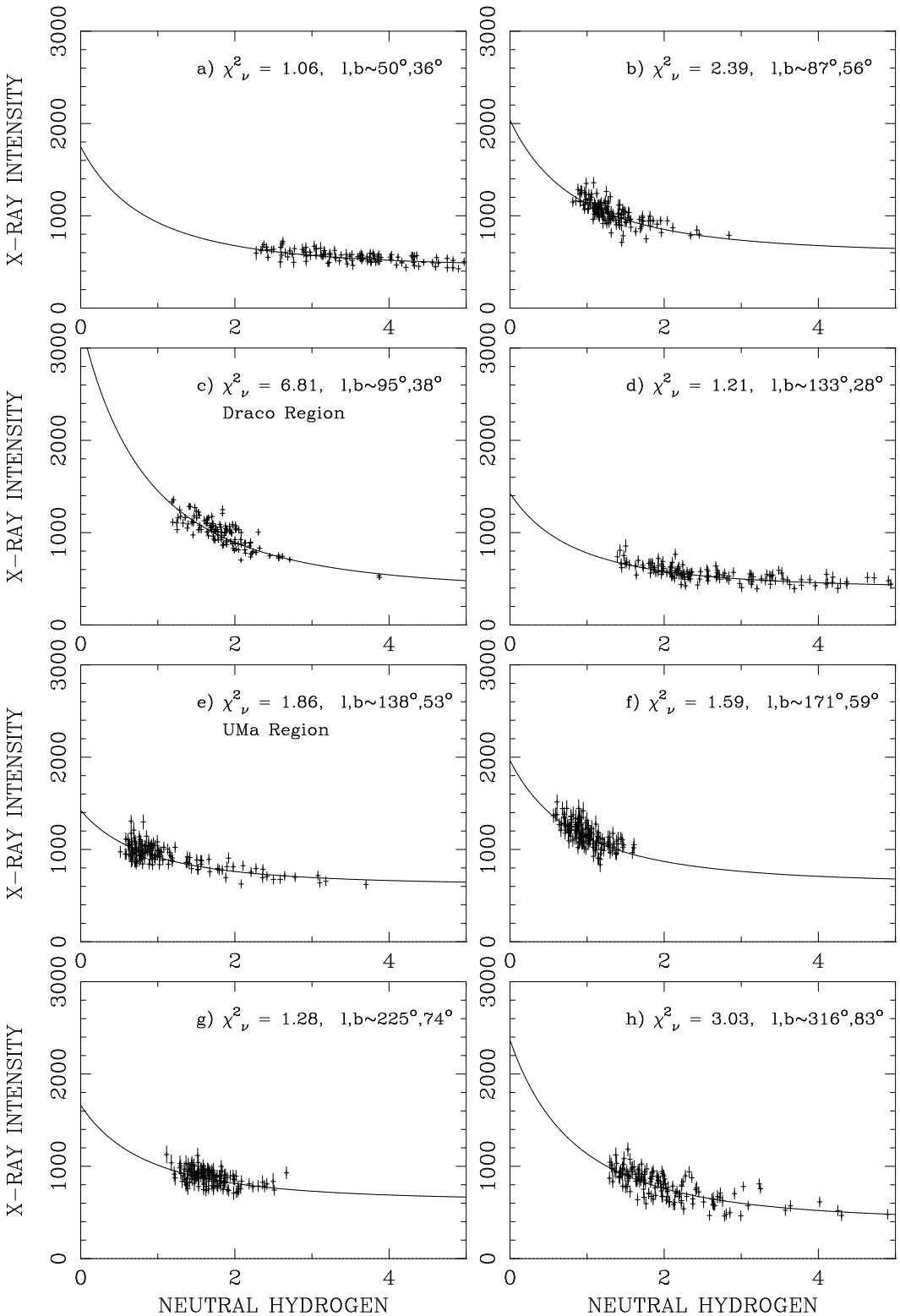

FIG. 5.—Scatter plots of observed R12 band intensity vs. corrected and scaled *IRAS* 100 μm intensity plus fitted model curves for eight representative regions. The χ^2_ν values for the fits are shown in the plots.

and are noted as being discrepant (see Snowden et al. 1995b, Fig. 6 for an identification of map features). They can contribute to either the fitted foreground or background components, or both, depending on the details of the distributions of the X-ray–emitting and X-ray–absorbing gas.

The fitting process results in maps of the foreground and background components on a 3°.2 × 3°.2 sample grid. We assume that the foreground component is smoothly varying over larger angular scales, and therefore we smooth with a 3 × 3 pixel sliding box after excluding extreme outliers (pixels that lie a factor of 2 above or below the average

value of the surrounding pixels). This exclusion affected only 0.4% of the R1 band pixels and 1.7% of the R2 band pixels. Pixels containing extreme outliers are replaced by the average of the surrounding pixels. The question of small-scale variations (less than a few degrees) is better treated by detailed investigations of more limited regions, preferably using pointed-observation data (see, e.g., Barber, Warwick, & Snowden 1996b; Park, Finley, & Snowden 1997; Kuntz, Snowden, & Warwick 1998). These studies suggest that there are $\sim 10\%$ variations in the I_0 flux on angular scales of a few degrees (which are likely contributors to the large χ^2_ν values).

For internal consistency, after determining an initial temperature for the distant emission (see § 3.2) we refitted the data with the appropriate absorption cross sections for a thermal emission spectrum of that temperature ($10^{6.02}$ K). This corrects for the slight dependence of the effective band-averaged absorption cross section on the specific spectrum.

3.1. *Foreground (LHB) Emission*

Figure 6*a* (Plate 25) shows an all-sky map of the fitted and smoothed values for the foreground component for the sum of the R1 and R2 bands (the $\frac{1}{4}$ keV band). Values for the foreground intensity span a factor of ~ 3.3 from ~ 250 to $\sim 820 \times 10^{-6}$ counts s^{-1} arcmin^{-2}, which implies emission measures of 0.0018–0.0058 cm^{-6} pc. Here and elsewhere in this paper, we assume thermal equilibrium emission for both local and halo components and use the 1991 vintage of Raymond & Smith (1977) spectra including the cosmic abundances of Allen (1973), which mainains consistency with Snowden et al. (1997) and other previous papers. The general appearance of the I_0 map is similar to that of the total background, with many of the same major features present: higher Galactic latitudes tend to have higher intensities, and the lower intensities are near the Galactic plane. The regions of highest intensity in the south (exclusive of the Eridanus Superbubble) are in the range $230° < l < 15°$, $-70° < b < -35°$, while in the north (exclusive of the Monogem enhancement and the North Polar Spur) the highest intensities are mostly in the range $90° < l < 210°, 40° < b < 70°$.

The strongest enhancement in the Galactic plane is due to "contamination" by the Monoceros-Gemini (Monogem; l, $b \sim 210°$, $10°$, diameter $D \sim 25°$) supernova remnant (e.g., Plucinsky et al. 1996). A second enhancement at (l, $b \sim 275°$, $20°$, $D \sim 20°$) is aligned with a low-latitude local minimum in $N_{\rm H}$ (see Snowden et al. 1997, Fig. 5*d*), which apparently provides a "window" to either the interior of Loop I or more distant emission. (Loop I [l, $b \sim 330°$, $20°$, $D \sim 115°$] is the neighboring SNR/stellar wind bubble surrounding the Sco-Cen OB association. First identified in the radio (Berkhuijsen, Haslam, & Salter 1971), it is a dominant feature in the Galactic center direction in X-rays, particularly above 0.5 keV; e.g., Egger 1995 and references therein.) Without them, the Galactic plane would appear considerably more uniform. The North Polar Spur (NPS; l, $b \sim 0°$, $70°$ to $\sim 25°$, $40°$; the limb-brightened northeastern edge of Loop I) and Eridanus Superbubble (l, $b \sim 200°$, $-40°$, $D \sim 20°$; e.g., Guo & Burrows 1997; Snowden et al. 1995a) produce similar excesses out of the plane.

Figure 6*b* shows an all-sky map of the R2/R1 band ratio for the foreground emission, while Figure 7*a* shows a histogram of the same data. For Figure 7, data from the Loop I, Monogem, and Eridanus regions are excluded from the distributions. Specifically, this removed data within 70° of (l, $b = 329°$, $17.^{\circ}5$), 15° of (l, $b = 205°$, $15°$), and 14° of (l, $b = 203°$, $-42°$), respectively. The distribution is well peaked at a value of ~ 1.12 with half-maximum values of 1.02 and 1.23. These ratios can be interpreted as model emission temperatures of $10^{6.07}$ K, $10^{6.02}$ K, and $10^{6.12}$ K, respectively, assuming no foreground absorption. The R2/R1 band ratio over the sky for the LHB emission is relatively consistent with a single-temperature plasma. However, there is still the suggestion of large-scale structure in Figure 6*b* that may be associated with thermal gradients or other emission variations in the LHB. In particular, the Galactic anticenter direction (exclusive of Eridanus and Monogem) appears on average to be slightly cooler, which is consistent with the results of Snowden, Schmitt, & Edwards (1991) using Wisconsin survey data (McCammon et al. 1983). However, the tightness of the distribution also indicates that our results are not strongly affected by systematics, as they would broaden the peak.

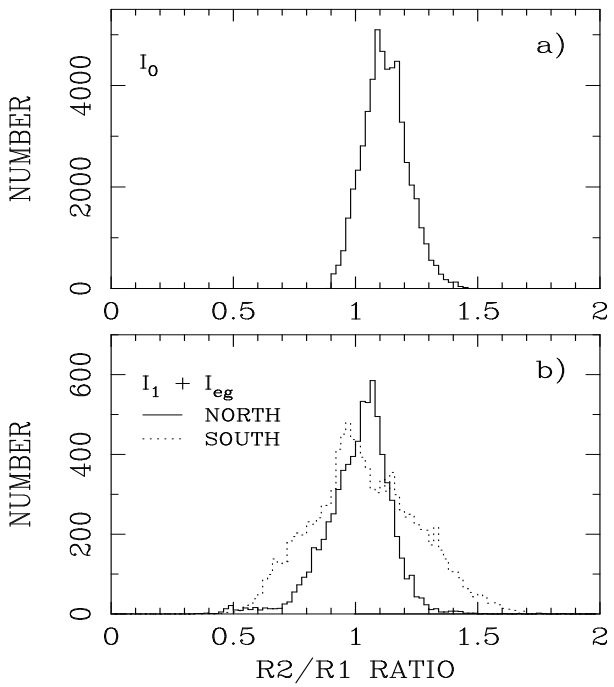

FIG. 7.—Histograms of R2/R1 band ratios. (*a*) Foreground component, I_0, from Fig. 6*b*. (*b*) Distant component, $I_{eg} + I_1$, from Figs. 8*a* and 8*b*. The solid line in (*b*) shows the northern hemisphere data, while the dashed line shows the southern hemisphere data. The vertical scaling is arbitrary as the plots oversample the data. Data from distinct features (e.g., Loop I; see text) are excluded.

A few additional enhancements along the Galactic plane need to be considered. (1) The slight intensity enhancement and associated spectral hardening at $l \sim 70°$ ($D \sim 40°$) is in the direction of the Cygnus Loop, the Cygnus Superbubble, and the Orion-Perseus interarm region. While the Cygnus Loop has been excluded from the fitted data set and the Cygnus Superbubble is ~ 1 kpc distant, this suggests the existence of emission originating beyond the LHB and local cavity that is apparently bright enough and/or the foreground column densities low enough that some of the absorption-hardened flux is still observed. This could largely be due to the response, albeit small, of the R2 band around 0.5 keV (Fig. 1). (2) The enhancement at l, $b \sim 255°$,

$-15°$ ($D \sim 30°$) may be associated with the third-quadrant void, the direction of greatest extent of the local cavity in the Galactic plane, and will be discussed below. (3) The low surface brightness bridge between the northern and southern hemispheres at $l \sim 125°$ is likely due to residual errors in the survey data reduction as it coincides with a separate survey interval and runs parallel to the scan path (1991 August; see Snowden et al. 1995b). Again, we have left the regions affected by large-scale distinct features in the maps because they are typically fully resolved, but we have excluded their effects from further analysis. Outside of these regions, the brightest areas are not at the Galactic poles but are still at relatively high latitudes. The dimmest region is in the second quadrant south of the Galactic equator.

3.2. *Distant (Halo and Extragalactic) Emission*

Assuming that we have accurately determined the foreground emission, I_0, it is a simple matter to determine the magnitude and effective temperature of the distant component, $I_{\rm dist} = I_{\rm eg} + I_1$. However, instead of using the fitted values for I_1, which have errors that are highly correlated with the errors of I_0 but are greater in magnitude, we use our smoothed I_0 map to evaluate the inverted equation:

$$I_{\rm dist} = I_{\rm eg} + I_1 = I_{\rm eg} + \{I_{\rm X} - I_0 - I_{\rm eg} \times \exp\left[-\sigma(N_{\rm H}, \alpha) \times N_{\rm H}\right]\}/\exp\left[-\sigma(N_{\rm H}, T) \times N_{\rm H}\right] .$$

Figures 8*a* and 8*b* (Plate 26) show the R2/R1 band ratio in the polar regions for the distant emission, while Figures 8*c* and 8*d* show the unabsorbed intensity of the $\frac{1}{4}$ keV band emission. Note that the large enhancement in the lower right of Figure 8*c* is caused by the NPS, while the enhancement in the lower right-hand part of Figure 8*d* is caused by Eridanus Superbubble. (For comparison, Figs. 8*e* and 8*f* show the SFD data for the same fields.) For these figures, we have masked data in which the absorbing column is >3.5 optical depths (i.e., $<5\%$ transmitting, $>4.5 \times 10^{20}$ H cm^{-2}). The distribution of the R2/R1 band ratio in the polar regions differs slightly between north and south (see Fig. 7*b*, again excluding the regions contaminated by the Loop I, Monogem, and Eridanus enhancements). While both peak at R2/R1 $\sim$ 1.01, the northern distribution is narrower than that in the south. Combining the two distributions, the half-maxima are at 0.86 and 1.17 (temperatures of $10^{6.02}$ K, $10^{5.94}$ K, and $10^{6.10}$ K, respectively).

3.2.1. *The Distribution of the Halo Emission*

The unabsorbed $\frac{1}{4}$ keV band halo plus extragalactic intensities in the north away from Loop I have values ranging between ~ 400 and $\sim 3000 \times 10^{-6}$ counts s^{-1} arcmin^{-2}. Subtracting our assumed extragalactic contribution leaves a halo intensity of $\sim$0–2600×10^{-6} counts s^{-1} arcmin^{-2}, emission measures of $\sim$0–0.017 cm^{-6} pc (assuming thermal equilibrium emission). The values in Ursa Major, $\sim 700 \times 10^{-6}$ counts s^{-1} arcmin^{-2}, are consistent with those derived by Snowden et al. (1994a) in their more detailed analysis of the Lockman Hole region (the direction of the minimum column density of Galactic H I). Similarly, the values in the Draco Nebula region, $\sim 2600 \times 10^{-6}$ counts s^{-1} arcmin^{-2}, are reasonably consistent with those derived by Snowden et al. (1991) and Moritz et al. (1998). This provides an estimate of the reliability of our procedures, even in directions of relatively high optical depths, sharp gradients in the emission measure of the foreground or halo emission, and/or the presence of molecular gas. (We note that our modeling for the Draco region had relatively high χ^2_ν values indicating statistically poor fits to the data, partly due to the larger values of I/σ_I near the ecliptic poles.)

The distant emission in the south is fairly flat near the pole with values between ~ 500 and $\sim 1200 \times 10^{-6}$ counts s^{-1} arcmin^{-2}. It increases from the pole up to intensities of a few thousand closer to the plane. This is qualitatively consistent with the latitude dependence of a plane-parallel distribution of the emitting material over the visible region of the halo but is quantitatively too great an increase.

3.2.2. *The Temperature of the Halo Emission Reconsidered*

Our values for the temperature of the halo emission responsible for the $\frac{1}{4}$ keV band flux are well away from the value of $\sim 10^{6.3}$ K, with a R2/R1 band ratio of 1.37, suggested by some other studies (e.g., Wang & McCray 1993; Kerp 1994). Our values are also different from the more recent results of Sidher et al. (1996) which reports a value of $10^{6.4}$ K (using the Raymond & Smith 1977 plasma code similar to that used in this paper, and $10^{6.2}$ K using the Landini & Monsignori Fossi 1990 code) for the halo emission derived from *ROSAT* pointed observations. We suggest that the discrepancy arises from the previous use of a single-temperature emission model to fit what is at least two distinct components: the low-temperature component considered in this paper, which is responsible for most (and in this paper all) of the halo emission observed at $\frac{1}{4}$ keV, and a hotter component, which is used to explain the observed excess at $\frac{3}{4}$ keV over the extrapolation of the extragalactic background observed at higher energies. While one temperature can be forced to fit the data for a given direction, the requirement for at least two components is supported by the difference in angular structure between the variable and occasionally clumpy $\frac{1}{4}$ keV halo emission (Figs. 8*c* and 8*d*) and the rather smooth intensity distribution at $\frac{3}{4}$ keV outside of Loop I (see, e.g., McCammon & Sanders 1990; Snowden et al. 1995b).

To examine the problem quantitatively, for the bright halo regions ($\sim 2000 \times 10^{-6}$ counts s^{-1} arcmin^{-2} at $\frac{1}{4}$ keV), a $10^{6.3}$ K plasma would produce $\sim 260 \times 10^{-6}$ counts s^{-1} arcmin^{-2} in the $\frac{3}{4}$ keV band. This is 2 times greater than the observed rates ($\sim 130 \times 10^{-6}$ counts s^{-1} arcmin^{-2}) typical for high-latitude directions away from the Galactic center region, where at least one-third is known to be extragalactic (Hasinger et al. 1993). This argument can be continued to show the consistency of the model presented here. A 10^6 K plasma with an emission measure that produces 2000×10^{-6} counts s^{-1} arcmin^{-2} in the $\frac{1}{4}$ keV band produces only 13×10^{-6} counts s^{-1} arcmin^{-2} in the $\frac{3}{4}$ keV band. The variation of the $\frac{1}{4}$ keV distant emission ($\sim 1500 \pm 1000 \times 10^{-6}$ counts s^{-1} arcmin^{-2}) thus only produces a variation of about 10% in the $\frac{3}{4}$ keV band, an amount that is easily hidden in the survey data. The $E^{-1.96}$ power law that produces our assumed 400×10^{-6} counts s^{-1} arcmin^{-2} in the $\frac{1}{4}$ keV band provides $\sim 40\%$ of the observed $\sim 130 \times 10^{-6}$ counts s^{-1} arcmin^{-2} in the $\frac{3}{4}$ keV band. A plasma with a temperature of $10^{6.4}$ K was used by Nousek et al. (1983) to provide the excess emission at $\frac{3}{4}$ keV over an $11E^{-1.4}$ photons cm^{-2} s^{-1} sr^{-1} keV^{-1} extragalactic power law. At this temperature, an emission measure that produces the additional $\sim 80 \times 10^{-6}$ counts s^{-1} arcmin^{-2} observed $\frac{3}{4}$ keV band intensity produces only $\sim 270 \times 10^{-6}$ counts s^{-1} arcmin^{-2} in the $\frac{1}{4}$ keV band.

Again, this amount can be hidden in the derived distant emission of this paper, and it could be reduced by an additional factor of 2 by increasing the temperature to $10^{6.5}$ K. The all-sky analysis of the *ROSAT* $\frac{3}{4}$ keV band data will be presented in subsequent papers (see, e.g., Freyberg et al. 1998).

We note that the choice of two isothermal components to produce the $\frac{1}{4}$ keV and $\frac{3}{4}$ keV observed excesses over the extrapolation of the extragalactic power law is almost certainly a simplification of the halo conditions. The halo emission more likely originates from plasmas with a distribution of temperatures.

3.2.3. *Checks on the Analysis*

As a check for possible biases in our results, we examined our derived distant unabsorbed intensities as a function of absorbing N_H for any global correlation. Such a correlation could imply that our deabsorption technique produces systematic artificial structure in the halo emission. Figure 9 shows the results for the northern and southern poles separately for $b > 65°$. The northern data show increased scatter with increasing N_H but no other general trend. The southern data show a bimodal distribution with flat distributions above and below a slight break at 1.4×10^{20} H cm^{-2}. Thus there is little indication of any significant correlation or biasing. This is the case even though some correlation would be expected if the halo emission is distributed as a layer parallel to the Galactic disk, as both the X-ray intensity and H I column density would then tend to increase with decreasing Galactic latitude. Note that the column density range spans a couple of optical depths so any errors would likely be obvious.

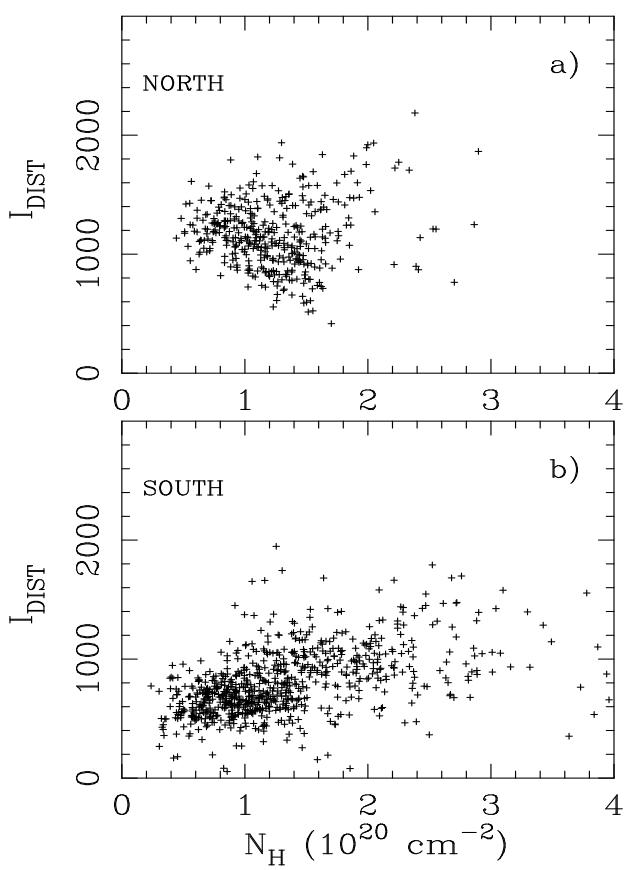

FIG. 9.—Scatter plot of N_H vs. $I_{dist} = I_{eg} + I_1$ for the (*a*) northern and (*b*) southern polar regions ($|b| > 65°$). The units of I_{dist} are 10^{-6} counts s^{-1} arcmin^{-2}.

To test the reasonableness of our model distributions of X-ray–absorbing and X-ray–emitting gas (foreground component plus background component absorbed by the total column density of H I) with a completely independent data set, we have compared them to the Wisconsin B-band data (0.13 − 0.188 keV) of McCammon et al. (1983) for the polar regions (excluding the bright emission of Loop I and Eridanus). We first compared the B-band data to a fitted scaling of the total R1 + R2 band intensity using average values over 24° circular regions. This essentially assumes that all of the $\frac{1}{4}$ keV SXRB originates within the LHB so that there is no spectral variation. There were 109 such regions with a χ^2 value of 675. We next compared the B-band data to model values derived by scaling the I_0 and $I_1 + I_{eg}$ maps. Specifically, the I_0 and $I_1 + I_{eg}$ maps were scaled by appropriate B-band/R12-band emission ratios and summed after absorption of the scaled $I_1 + I_{eg}$ data using B-band cross sections and the total column density of Galactic H I. This creates a model B-band map based on the results of this paper. With this model the χ^2 value was reduced to 522. While neither scaling provided an acceptable fit, the reduction in the χ^2 value by 23% strongly suggests that our model is generally correct.

4. DISCUSSION

4.1. *The LHB and the $\frac{1}{4}$ keV SXRB*

Although the LHB looks quite similar in appearance to the model of a decade ago (see, e.g., Cox & Snowden 1986; Cox & Reynolds 1987; SCMS), this similarity is in spite of the revolution in our understanding of the $\frac{1}{4}$ keV SXRB brought about by observations of significant diffuse X-ray emission in the Galactic halo.

Following our model, the I_0 intensity map can be interpreted as a map of emission from the LHB, which in turn can be interpreted as a map of the radial extent of the LHB, but it is necessary to fix the distance scale in some way. The MBM 12 ISM absorption-line results (Hobbs, Blitz, & Magnani 1986) and X-ray shadowing results (Snowden, McCammon, & Verter 1993) constrain the scaling. Hobbs et al. (1986) placed the distance to MBM 12 at 65 ± 5 pc, using the stars HD 18404 and HD 18519/20. However, *HIPPARCOS* results (ESA 1997) for the distances to the two stars are 32 pc and 90 pc, respectively (rather than the 60 pc and 70 pc spectroscopic distances). Allowing a couple parsecs for the Local Cloud and using the R12 band intensity foreground to MBM 12 of 385×10^{-6} counts s^{-1} arcmin^{-2} (Snowden et al. 1993) yields a range of scales of 0.08–0.23 pc (10^{-6} counts s^{-1} arcmin^{-2})$^{-1}$. With this range of scale factors applied to the data of Figure 6*a*, the LHB has an extent of ~20–65 pc (low scaling) to ~60–190 pc (high scaling) depending on direction. The upper end of this range is consistent with the minimum scaling of SCMS. For the rest of this paper unless otherwise noted, the middle scaling of 0.155 pc (10^{-6} counts s^{-1} arcmin^{-2})$^{-1}$, which implies an LHB extent of ~40–130 pc, will be used.

Figures 10 and 11 show cuts of the LHB extent using the middle scaling of the data in Figure 6*a*. This scaling translates to a pressure of $P/k \sim 15{,}000$ cm^{-3} K, consistent with other measurements of the LHB pressure (see, e.g., Guo & Burrows 1997; Kuntz, Snowden, & Verter 1997; Berghöfer et al. 1997). Figure 12 shows a scatter plot of the present

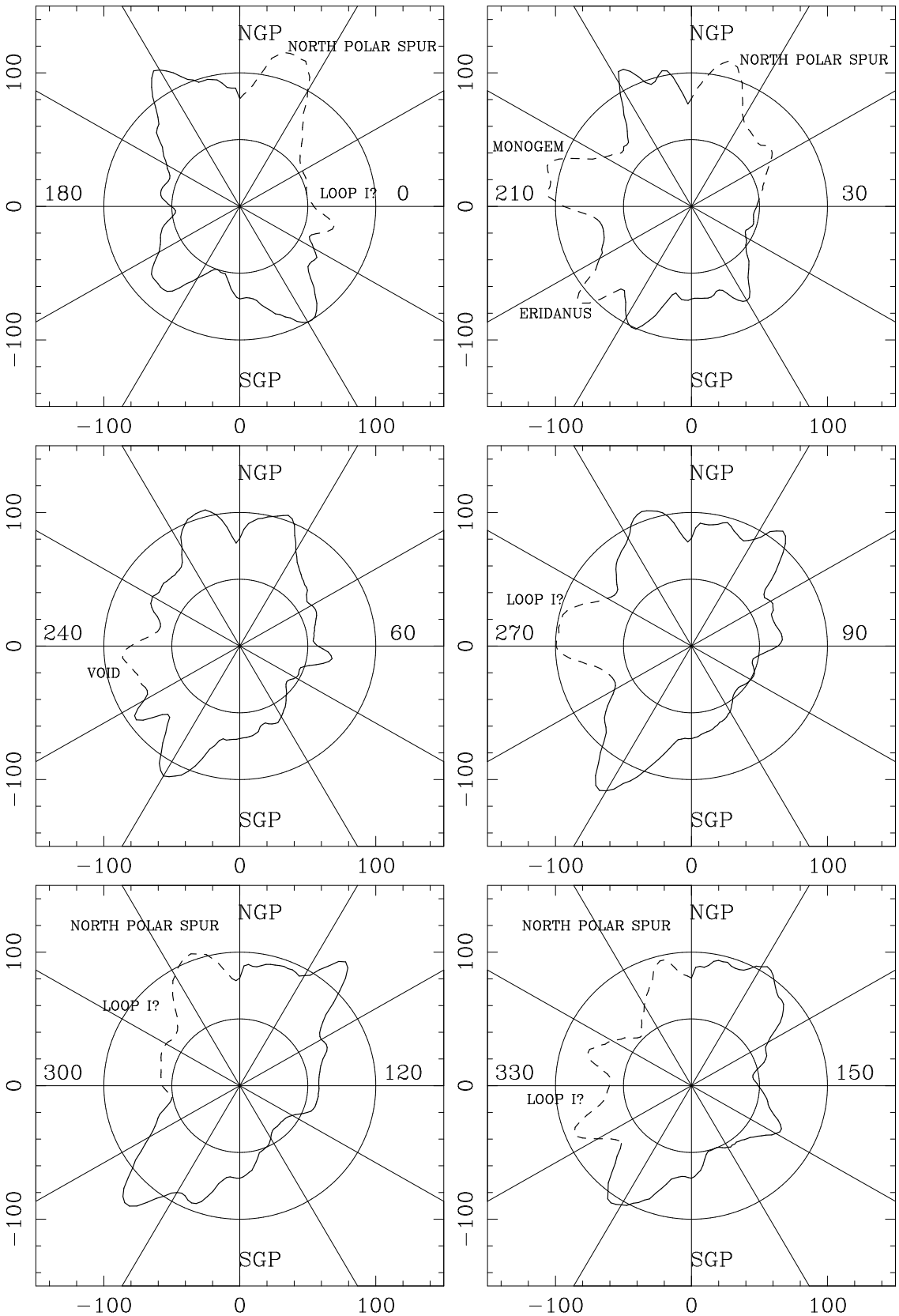

FIG. 10.—Plots of the LHB radius in great-circle cuts through the Galactic poles along the labeled longitudes. The radii are derived from the data in Fig. 6*a*: $R_{\rm LHB} = 0.155 \times I_0$. The scale circles have radii of 50 pc and 100 pc. Regions that are contaminated by discrete features or are of other interest are labeled and the curves dashed.

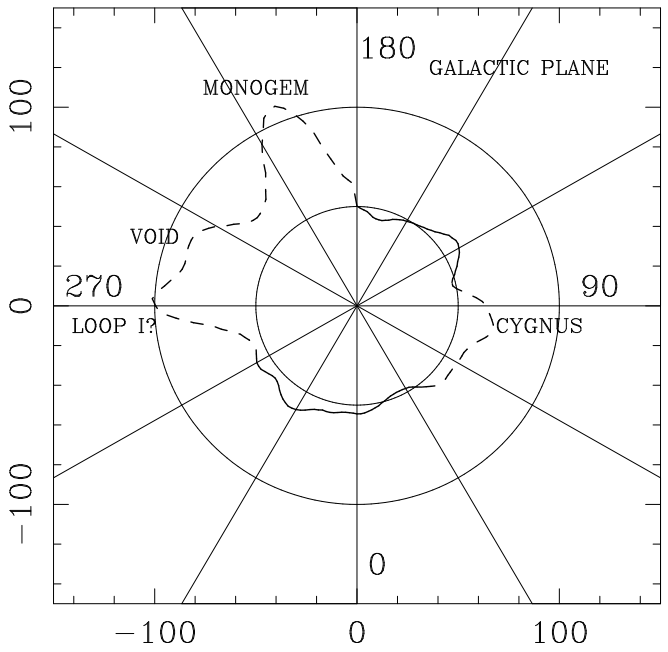

FIG. 11.—Plot of the LHB radius along the Galactic plane. The radii are derived from the data in Fig. 6*a*: $R_{\rm LHB} = 0.155 \times I_0$. The scale circles have radii of 50 pc and 100 pc. Regions that are contaminated by discrete features or are of other interest are labeled and the curves dashed.

LHB radius compared to that of SCMS excluding the Loop I, Eridanus, and Monogem regions. The line shows the average ratio for data with $|b| < 15°$, which should be unaffected by any residual halo contribution. That the inferred shape of the LHB is rather similar to that suggested by SCMS should not be surprising. The 1990 paper used the Wisconsin B-band (McCammon et al. 1983), which is less sensitive than the *ROSAT* $\frac{1}{4}$ keV band to emission in the Galactic halo as the absorbing optical depths are about twice as large (a minimum of 1 optical depth over a small area in Ursa Major, and more typically 2 or 3 optical depths even at high latitude). As expected, the directions on the sky that show the greatest excess of the SCMS radii over those of the present work are in directions of the highest count rates/lowest column densities, where the residual transmitted B-band flux from the halo and beyond is significant.

Figure 13 shows a scatter plot of the Be-band data (0.70–0.111 eV) from Bloch et al. (1986), Juda (1988), Juda et al. (1991), and Edwards (1990) versus the $\frac{1}{4}$ keV band I_0 intensity. The line shows the uncertainty-weighted average ratio for the points. For the Be band, the hydrogen column density at 1 optical depth is $\sim 10^{19}$ cm^{-2}, which implies that the Be band should sample *only* the emission from the LHB, and that the Be-band and I_0 data should be tightly correlated. The two points noted by circles that lie significantly below the line are contaminated at least at $\frac{1}{4}$ keV by the Monogem enhancement, which can explain their deviations. Without the contamination, the I_0 intensities would likely be $\sim 400 \times 10^{-6}$ counts s^{-1} arcmin^{-2} (typical values nearby in the Galactic plane), which would bring the two points into agreement with the line. The other two points noted by circles lie in regions affected by emission from the NPS. The fact that they still lie close to the line even though the I_0 data are affected by emission from the NPS is interesting and suggests that there is little H I separating Loop I and the LHB in this region (see Cox & Reynolds 1987). The average ratio in the plot was calculated excluding these four points and yields a χ^2_ν value of 1.46, a $\sim 10\%$ probability for 20 degrees of freedom. Including the four points yielded $\chi^2_\nu = 2.08$.

It must be noted, however, that the extent of the LHB is not necessarily the extent of the local cavity in the H I of the Galactic disk. In some directions, most notably in the direction of β CMa (l, $b = 226°$, $-14°$, $d = 203$ pc) in the third quadrant, the cavity extends $\gtrsim 200$ pc (e.g., Paresce 1984; Welsh et al. 1994) while the LHB, using the middle scaling of the I_0 X-ray intensity, extends only to ~ 60–95 pc. Note that the results of Gry, York, & Vidal-Madjar (1985) indicate that H II gas fills in at least some of the otherwise vacant line of sight. To investigate this issue further, we have used the Na I ISM absorption-line data of Welsh et al. (1994, and references therein) to compare the size of the cavity with the extent of the LHB. (Owing to the paucity of appropriate target stars, high Galactic latitudes are poorly sampled for distances $\gtrsim 100$ pc.) Figure 14 shows a scatter

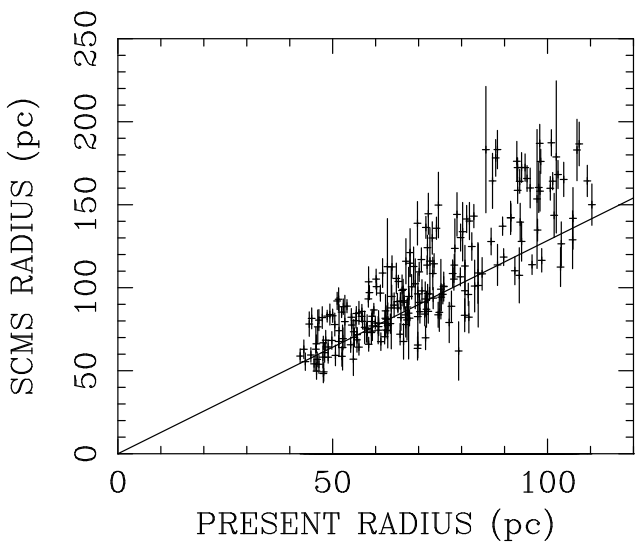

FIG. 12.—Scatter plot of SCMS radii for the LHB vs. the radii from this paper. The SCMS radii are derived using their scale factor assuming the highest electron density. The line shows the average ratio for $b < 15°$.

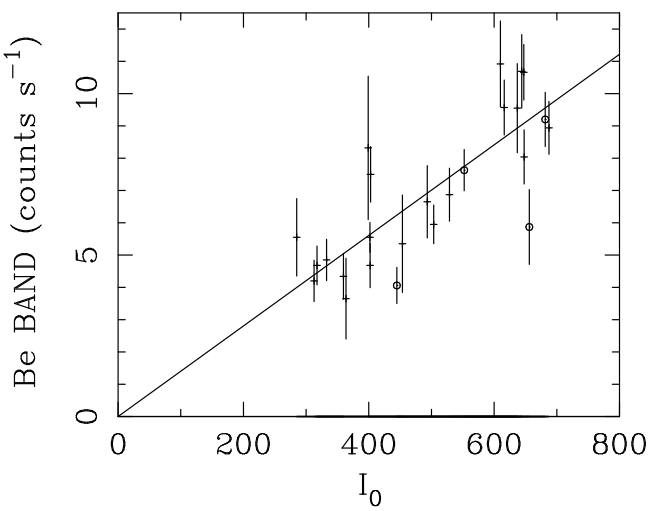

FIG. 13.—Scatter plot of Juda et al. (1991) Be band (0.70–0.111 keV) data vs. I_0. The I_0 intensity has been calculated using a triangular response of 15° FWHM. The line shows the average ratio for the points.

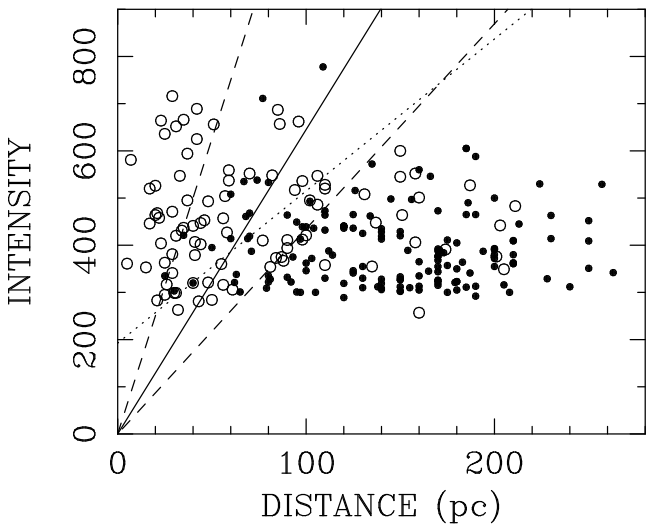

FIG. 14.—Scatter plot of the distance to the stars of Welsh et al. (1994) vs. the $\frac{1}{4}$ keV intensity in the direction of the stars. Stars presumably within the cavity (foreground $N_{\rm Na\,I} < 10^{10.3}$ cm^{-2} or $N_{\rm H} \lesssim 5 \times 10^{18}$ cm^{-2}) are indicated by open symbols and stars outside of cavity ($N_{\rm Na\,I} > 10^{11.0}$ cm^{-2} or $N_{\rm H} \gtrsim 2 \times 10^{19}$ cm^{-2}) are indicated by filled symbols. The solid and dashed lines show the LHB radius vs. $\frac{1}{4}$ keV I_0 intensity relations of § 4.1; the dotted line shows that for § 4.2. The $\frac{1}{4}$ keV intensity is in units of 10^{-6} counts s^{-1} arcmin^{-2}.

plot of the distance to the stars versus the $\frac{1}{4}$ keV intensity in the direction of the stars, with different symbols indicating whether the star is inside or outside the cavity. The solid line indicates the distance to the edge of the LHB as a function of $\frac{1}{4}$ keV intensity using the 0.155 pc (10^{-6} counts s^{-1} arcmin^{-2})$^{-1}$ scaling. The dashed lines show the effect of scaling by 0.08 pc (10^{-6} counts s^{-1} arcmin^{-2})$^{-1}$ (steeper) and 0.23 pc (10^{-6} counts s^{-1} arcmin^{-2})$^{-1}$. The flatter scaling appears to be ruled out by the data, but scaling by values $\lesssim$0.15 pc (10^{-6} counts s^{-1} arcmin^{-2})$^{-1}$ is reasonable.

If our model is correct, stars above the lines should be within the LHB and cavity, and stars below the line should be outside of the LHB but may or may not be outside of the cavity. Figure 15 shows an Aitoff-Hammer projection of the positions of the Welsh et al. (1994) stars with different

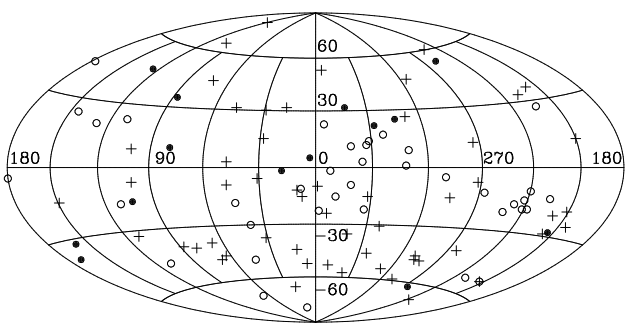

FIG. 15.—Plot of the positions of the Welsh et al. (1994) stars in Galactic coordinates in an Aitoff-Hammer projection. Plus signs indicate stars where the model agrees with the data; i.e., either the star has $< 5 \times 10^{18}$ cm^{-2} of foreground absorption and a distance that places it in the LHB, or the star has $> 2 \times 10^{19}$ cm^{-2} of foreground absorption and a distance that places it outside of the LHB. Open circles indicate stars with distances placing them outside of the LHB but that have foreground columns $< 5 \times 10^{18}$ cm^{-2}. Filled circles indicate stars with distances placing them inside of the LHB but that have foreground columns $> 2 \times 10^{19}$ cm^{-2}.

symbols depending on whether the data and model agree or disagree. (The middle scaling, i.e., 0.155 pc [10^{-6} counts s^{-1} arcmin^{-2}]$^{-1}$ is again used.) Except for 14 stars that have foreground column densities placing them outside the cavity but $\frac{1}{4}$ keV I_0 intensities and distances placing them within the LHB (*filled circles*) that are distributed fairly randomly across the sky, this appears to be the case. (Note that the discrepancies can arise, for example, from errors in the stellar distance, errors in the column density determinations, and foreground clouds in the LHB not resolved in our analysis.) There are, however, a significant number of stars (38) that the data imply are within the cavity but outside the LHB (*open circles*). About 60% of the latter group are found in two clusters, one centered near (l, $b \sim 340°$, 0°) and the other centered near the third-quadrant void (l, $b \sim 240°$, $-15°$). There are 55 stars that are consistent with the LHB completely filling the cavity.

The void in the third quadrant (e.g., Welsh et al. 1994 and references therein), or "region of bizarre emptiness" (RBE; Cox 1997) can be used to address the question of how common $\sim 10^6$ K plasma is in the disk of the Galaxy. If the neutral material of the disk is not significantly clumped, then on average we can sample at $\frac{1}{4}$ keV only the nearest hundred parsecs near the Galactic plane. The global filling factor of $\sim 10^6$ K plasma in the Galactic disk is then impossible to observe directly. However, in this one direction in the Galactic disk where we can see several hundred parsecs, there is no obvious strong enhancement of the $\frac{1}{4}$ keV background. The intensity at l, $b \sim 225°$, 0° is $\sim 425 \times 10^{-6}$ counts s^{-1} arcmin^{-2}, while the peak plane intensity in the neighborhood, at (l, $b \sim 250°$, 0°), is $\sim 600 \times 10^{-6}$ counts s^{-1} arcmin^{-2}. Both of these can be compared to a nominal plane intensity of $\sim 300 \times 10^{-6}$ counts s^{-1} arcmin^{-2}, and the intensities correspond to emission path lengths of 95 pc, 65 pc, and 45 pc, respectively. This implies that at $l \sim 225°$, there are at most only 20 pc of additional 10^6 K plasma beyond the LHB (assuming that the LHB extends only to the nominal 45 pc). Since the cavity extends beyond 200 pc (the distance to β CMa), this implies that the filling factor of plasma outside the LHB in this direction is $\lesssim$0.1. At $l \sim 250°$, the limit is $\lesssim$0.3. Both of these values are conservative upper limits as the cavity extends farther than 200 pc and the LHB quite possibly extends farther than 45 pc, if not to the full 65 pc and 90 pc. We note that a plasma path length of 200 pc (filling the cavity with hot plasma) would produce an intensity of $\sim 1430 \times 10^{-6}$ counts s^{-1} arcmin^{-2}. This is certainly not a conclusive argument against a large filling factor of $\sim 10^6$ K plasma in the Galactic disk, but models that postulate a large filling factor must also explain why it is low in the one direction where it could be easily observed.

"Plugging" the RBE with ionized hydrogen and neutral or singly ionized helium would absorb some distant flux but would require an extensive path length, and therefore a large filling factor, and would still exclude the hot plasma. Such gas at 20,000 K and in thermal pressure equilibrium with the 10^6 K plasma would require a path length of $\sim$200 pc to achieve 1 optical depth at $\frac{1}{4}$ keV. An alternative to filling the RBE with H II gas is to fill it with a plasma with $T \gtrsim 10^{6.5}$ K (D. P. Cox 1997, private communication). Two hundred parsecs of this plasma with the same thermal pressure as the LHB would produce (using the same emission models as above) a $\frac{1}{4}$ keV band count rate of 40×10^{-6} counts s^{-1} arcmin^{-2} and a $\frac{3}{4}$ keV band count rate of

20×10^{-6} counts s^{-1} arcmin^{-2}. Both of these are at levels difficult to distinguish in the X-ray survey data.

4.2. *LHB Caveats*

We have made two special assumptions that warrant particular attention; that the $\frac{1}{4}$ keV emission in the LHB is distributed uniformly along the line of sight and that the spectrum of the emission is well characterized by thermal equilibrium models. However, many models for the emission from bubbles of hot plasma show significant edge brightening (e.g., Slavin & Cox 1992). The existence of such emission would affect, among other things, the distance scale of the LHB. For instance, if half of the intensity in the direction of MBM 12 originates in the boundary layer at the edge of the LHB and if the boundary-layer emission is constant across the sky, the distance scale would then be $D = (I_0 - 192.5) \times 0.31$ pc (assuming the original scaling of 0.155 pc [10^{-6} counts s^{-1} arcmin^{-2}]$^{-1}$), where I_0 is in units of 10^{-6} counts s^{-1} arcmin^{-2}. This would change the range of the LHB extent to $\sim$20–195 pc (from $\sim$40–130 pc). Both the electron density and pressure of the interior plasma would be reduced by a factor of $2^{1/2}$ ($n(e) \sim 0.005$ cm^{-3}, $P/k \sim 10{,}600$ cm^{-3} K). The dotted line in Figure 14 shows this relation between LHB radius and $\frac{1}{4}$ keV intensity. As can be seen, this is reasonably consistent with the data. Any cooler material distributed in the LHB, such as the low-density clouds surrounding the Sun (see, e.g., Frisch 1995), displaces the X-ray–emitting plasma and affects the inferred shape of the LHB.

We also know from direct measurements that the LHB spectrum is not at all well fitted by the thermal equilibrium models we have used here (Sanders, Edgar, & Liedahl 1996). However, as yet, no other models work, either (nonequilibrium and/or variation in abundances, although progress is being made; Sanders 1997), so we continue to use the old standards to facilitate comparisons with earlier work. This adds to the uncertainty of derived parameters such as temperature, density, and pressure.

As a final caveat, we have built into the model that the local component is smoothly varying over angular scales of $\lesssim 10°$, and this analysis is insensitive to any variation on finer scales.

4.3. $\frac{1}{4}$ keV *Emission in the Galactic Halo*

Except for a limited number of regions such as Draco, the North Polar Spur, and southern latitudes with $b > -45°$, the derived halo emission of $\frac{1}{4}$ keV X-rays varies over the range $\sim$200–1500 $\times 10^{-6}$ counts s^{-1} arcmin^{-2} and is relatively isothermal (at least some of the temperature variation is likely due to limitations in the analysis technique). The Draco region, however, shows a strong intensity enhancement over a relatively limited solid angle ($\sim$0.03 sr). This enhancement, the first unambiguous Galactic halo emission discovered (Burrows & Mendenhall 1991; Snowden et al. 1991), has led to a biased view of the clumpiness of the halo emission as well as to an overestimate of the mean halo surface brightness.

The halo emission is brighter in the region of the north Galactic pole than the south, while halo emission in the south increases more strongly toward lower latitudes. The longitude dependence at lower latitudes is considerably different in appearance between the northern and southern hemispheres as well, although this is dominated by the effect of distinct features such as the North Polar Spur in the north and Eridanus in the south.

The average values for the distant emission for latitudes $b > 65°$ are 1545×10^{-6} counts s^{-1} arcmin^{-2} for the north and 810×10^{-6} counts s^{-1} arcmin^{-2} for the south. After subtraction of the assumed extragalactic contribution, they are reduced to 1145 and 410×10^{-6} counts s^{-1} arcmin^{-2}. Thus the southern value lies well within the range of LHB emission, while the northern value is only a factor of $\sim$1.4 larger than peak LHB values.

The average values for the halo emission in the polar regions are roughly a factor of 2 lower than the $\frac{1}{4}$ keV surface brightness of the face-on spiral galaxy M101 at the equivalent position of the solar circle: $\sim 1570 \times 10^{-6}$ counts s^{-1} arcmin^{-2} (Snowden & Pietsch 1995). The sum of the average halo emission from $|b| > 65°$ corresponds to a luminosity of $\sim 6.6 \times 10^{36}$ ergs s^{-1} kpc^{-2}. Using values for Type I and Type II supernova rates and the average energy dumped into the interstellar medium by their explosions (and precursor winds for Type II supernovae) listed in Ferrière (1995), an average value of $\sim 8 \times 10^{38}$ ergs s^{-1} kpc^{-2} can be derived for near the solar circle. Thus the local halo emission at $\sim 10^6$ K constitutes $\sim$1% of the average supernova power at the solar circle. This is consistent with past estimates (e.g., $<3\%$; Cox 1981).

The surface brightness of the distant emission in a few regions both in the north and south is particularly low, $\lesssim 600 \times 10^{-6}$ counts s^{-1} arcmin^{-2}. If the presumed extragalactic background is subtracted, very little is left ($\lesssim 200 \times 10^{-6}$ counts s^{-1} arcmin^{-2}) that can be of halo origin, which again underscores the variation of the halo emission.

4.3.1. *A Cygnus Superbubble–Draco Halo Connection?*

It is interesting to consider the $\frac{3}{4}$ keV band intensity enhancement extending from the Cygnus Superbubble to near the Draco Nebula (see Snowden et al. 1997, Fig. 3f), which we will call the Cygnus-Draco Plume, with the assumption that it is associated with the $T \sim 10^6$ K plasma that backlights the Draco Nebula. At a latitude of $b \sim 30°$, the $\frac{3}{4}$ keV intensity is $\sim 158 \times 10^{-6}$ counts s^{-1} arcmin^{-2}, an enhancement of $\sim 30 \times 10^{-6}$ counts s^{-1} arcmin^{-2} over the nominal intensity at higher latitudes. The H I column density is $\sim 3.6 \times 10^{20}$ cm^{-2}, which absorbs $\sim$43% of the flux in the $\frac{3}{4}$ keV band from a $10^{6.02}$ K thermal-equilibrium plasma. The emission measure required to produce the observed $\frac{3}{4}$ keV band enhancement would also produce a $\frac{1}{4}$ keV band intensity of $\sim 6550 \times 10^{-6}$ counts s^{-1} arcmin^{-2}, which when absorbed would be reduced to $\sim 450 \times 10^{-6}$ counts s^{-1} arcmin^{-2}. The observed $\frac{1}{4}$ keV intensity at $b \sim 30°$ is $\sim 680 \times 10^{-6}$ counts s^{-1} arcmin^{-2}, an enhancement of $\sim 305 \times 10^{-6}$ counts s^{-1} arcmin^{-2} over the intensity at $b \sim 15°$ at slightly lower longitudes, and is within a factor of 1.5 of the required amount.

While more study needs to be done, the factor-of-2 consistency above does suggest that the $\frac{3}{4}$ keV band enhancement observed at higher latitudes above the Cygnus Superbubble is the high-energy tail of a strong plume of 10^6 K plasma. The northern end of this Cygnus-Draco plume is responsible for the $\frac{1}{4}$ keV halo enhancement observed behind the Draco Nebula. To be quantitative, the emission enhancement over a $15° \times 15°$ region at (l, $b \sim 80°$, $30°$), which excludes the brightest emission of the Superbubble at lower latitudes, implies a flux of $\sim 2.6 \times 10^{-8}$ ergs s^{-1} cm^{-2}. If the enhancement is at the

distance of the Cygnus Superbubble (~ 1 kpc), the luminosity for the region would be $\sim 3 \times 10^{36}$ ergs s^{-1}.

We note in passing that there is an alternative explanation for the emission for the Cygnus Superbubble. It has been suggested that the "superbubble" is actually the superposition of a number of distinct SNRs distributed along the interarm region (e.g., Bochkarev & Sitnik 1985). While this may more accurately reflect the true distribution of emission, either way there is a strong enhancement of hot plasma in this direction which can be the source of the plume.

4.4. *Halo Caveats*

The interpretation of the halo emission comes with even more caveats than that of the foreground emission. Uncertainties in the spectral models, the possible clumping of absorbing material, the band-averaged absorption cross sections, the true extragalactic contribution, and possible additional absorption due to the Reynolds layer could all be important. As for the foreground emission, the thermal emission models are probably unrealistic, but changes in the fitted temperature do indicate differences in the spectral hardness.

Clumping of the X-ray–absorbing material reduces the effective absorption cross section and would therefore reduce the inferred halo intensity. However, a number of H I studies have indicated that the absorbing material is not clumped significantly enough to have a major effect on our analysis (Jahoda et al. 1985; Jahoda, McCammon, & Lockman 1986; Lockman, McCammon, & Jahoda 1986), so we can perhaps legitimately ignore that uncertainty.

While the extragalactic contribution at $\frac{1}{4}$ keV is constrained within a factor of ~ 2 by direct observations (Barber et al. 1996a and references therein), there is still some uncertainty in both its magnitude and spectral shape. In general, though, the magnitude of the halo contribution is considerably greater than the uncertainty in the extragalactic contribution, which implies that the observed variation of the halo emission is real.

4.5. *Comments on the Past*

An interesting historical question is why, given the existence of earlier soft X-ray sky surveys, it has taken so long to answer such a basic question as whether or not a significant part of the $\frac{1}{4}$ keV background comes from the Galactic halo, particularly as the general negative correlation of the X-ray background intensity with neutral hydrogen column density has been noted from its discovery (Bowyer et al. 1968) and has been analyzed in considerable detail since (e.g., McCammon et al. 1983; Marshall & Clark 1984; McCammon & Sanders 1990; Garmire et al. 1992).

Such a negative correlation suggests photoelectric absorption of an emission component originating behind the H I. However, the low values obtained for the apparent absorption cross sections and the almost complete lack of the expected energy dependence of these fitted cross sections required a degree of clumping of the absorbing material that could be ruled out by direct 21 cm measurements (Dickey, Salpeter, & Terzian 1978; Jahoda et al. 1985; Jahoda et al. 1986). The observed independence of intensity and spectrum inspired a model in which the negative correlation with H I was produced by displacement of H I by variations in the extent of a hot X-ray–emitting region surrounding the Sun (Sanders et al. 1977; McCammon et al. 1983; SCMS). Since such a region was required in any case by observation of a finite $\frac{1}{4}$ keV flux in the Galactic plane where the Galaxy is completely opaque, this model nicely satisfied Occam's razor by using the one region to produce *all* of the observed X-rays not contributed by distinct objects (e.g., SNRs) and by quite naturally predicting the lack of energy dependence in the H I negative correlation.

At the same time, the detailed negative correlation observed in some parts of the sky made it difficult to abandon the absorption picture (e.g., Marshall & Clark 1984). The apparent lack of energy dependence of this absorption could be approximated by suitable adjustments in the temperature of the distant component. However, measurements made in the Be band (Bloch et al. 1986; Juda et al. 1991; Edwards 1990), with an effective energy of ~ 100 eV and a band-averaged absorption cross section expected to be almost 10 times larger than for the $\frac{1}{4}$ keV band, showed approximately the same intensity variations and even with their limited statistical precision could not be accommodated by a simple absorption model (Bloch et al. 1986). The displacement geometry appeared to be the only model consistent with all of the available observations.

Early *ROSAT* observations of deep ($\sim 50\%$) shadows cast by small clouds located far above the galactic plane in Draco forced a reconsideration of this simple picture. A major result of the analysis presented here is the revealing of a variable distribution of the distant emission. The northern halo away from Draco and Loop I appears somewhat lumpy on an otherwise relatively flat distribution. This allowed for a fairly successful modeling of it as an isotropic background, particularly in the anticenter direction (Marshall & Clark 1984). The southern halo, however, has a strong gradient increasing toward lower latitudes, particularly in the Galactic center hemisphere. This more closely resembles a plane-parallel distribution of the halo emission. The difference between the northern and southern distributions would obviously cause problems with a symmetric halo, e.g., $I_X = I_0 + I_1 e^{-\tau}$ (isotropic) or $I_X = I_0 + I_1 \csc |b| e^{-\tau}$ (plane-parallel), where I_X is the observed intensity, I_0 is a constant foreground component, and I_1 is the scale factor for the background component absorbed by the optical depth τ. This analysis has allowed for a more direct measure of I_1 without forcing a specific geometry.

The same sorts of arguments are true for the local emission as well. Typically the foreground emission was modeled as a constant, as the data were insufficient to allow for constraining more creative distributions. The now-apparent factor-of-3 variation in the foreground emission would obviously cause such models severe problems. About half of the general plane-to-pole negative correlation observed between the $\frac{1}{4}$ keV background and Galactic H I still appears to be caused by displacement. This analysis also indicates a lower temperature for the halo component, so that after the spectral hardening produced by the absorbing gas, it has roughly the same observed spectrum as the unabsorbed LHB emission. These two effects dilute the remaining energy dependence of the absorption of the distant component to the point at which it could be accommodated by the limited statistical precision of the old B- and Be-band sounding rocket measurements and is still difficult to discern with the *ROSAT* data.

Investigating a model in which the foreground and background emission components are not fixed to a specific

geometry requires the huge improvement in statistics provided by the *ROSAT* all-sky survey. The angular resolution of these data allows the isolation of absorption-induced negative correlation from displacement by fitting only on angular scales that are too small for the displacement effect to operate. Another advantage of fitting for absorption only on small angular scales is that it minimizes the confusion caused by intrinsic variations of the background source emission.

Unfortunately, the only energy information available within the *ROSAT* $\frac{1}{4}$ keV data is the modest difference in effective energies of the R1 and R2 pulse-height bands (Fig. 1). While the precision of the data allows this to be used to obtain information on the emitting temperatures, it is too short a "lever" to provide a strong confirmation of the self-consistency of the model. New observations with a substantially lower effective energy and good statistical accuracy are needed. An investigation of even more complex models, in which part of the emission is intermixed with the absorbing material, will require independent distance measurements for a large number of absorbing clouds observed by *ROSAT*.

5. CONCLUSION

We have used the *ROSAT* all-sky survey data and *DIRBE*-corrected *IRAS* 100 μm data to study the distribution of emission responsible for the observed $\frac{1}{4}$ keV diffuse background. We find that emission from the LHB dominates the background at low Galactic latitudes and contributes much of the observed flux at high latitudes as well. The emission temperature of the LHB is in the range $10^{6.07\pm0.05}$ K, and the intensity varies between ~ 250 and 820×10^{-6} counts s^{-1} arcmin^{-2}. The intensity of the LHB emission can be used to estimate its radial extent from the Sun, which varies between 40 and 130 pc. These variations are strongly anticorrelated with total H I column density, presumably due to displacement effects as discussed in Sanders et al. (1977), McCammon & Sanders (1990), and SCMS. The LHB extends farther toward the Galactic poles than in the plane, although the regions of greatest extent are not at the poles themselves. We find no strong enhancement in the direction of the third quadrant void (RBE), which implies that it is not filled with 10^6 K plasma in thermal pressure equilibrium with the LHB.

Consistent with previous shadowing studies, we find extensive $\frac{1}{4}$ keV emission in the Galactic halo. The emission temperatures are in the range $10^{6.02\pm0.08}$ K, and the derived intensity outside the absorbing layer varies from near zero to $>3000 \times 10^{-6}$ counts s^{-1} arcmin^{-2}. Also consistent with previous studies, we find that the halo emission can vary by a factor of 2 over angular scales of $\sim 20°$. The average halo unabsorbed intensity in the south polar region is $\sim 410 \times 10^{-6}$ counts s^{-1} arcmin^{-2}, which is comparable to typical values for the LHB emission. The average value for the north polar region is $\sim 1140 \times 10^{-6}$ counts s^{-1} arcmin^{-2}, which is about 1.4 times the peak values for the LHB emission. Thus while there are some halo regions that are a factor of 4 or so brighter than the brightest LHB regions (e.g., Draco), more typical high-latitude values are similar to those in the LHB.

We have also identified an emission enhancement connecting the Cygnus Superbubble and Draco regions. This Cygnus-Draco Plume could originate in the Superbubble and then provide a source for the plasma responsible for the bright $\frac{1}{4}$ keV halo emission that backlights the Draco Nebula.

We would like to thank the referee, Don Cox, for his insightful, if blunt, comments that led to a number of significant improvements in this paper. We would also like to thank our colleagues K. Kuntz, D. McCammon, W. T. Sanders, R. Shelton, and R. S. Warwick for useful discussions and D. Schlegel and M. Davis for providing the SFD data before publication. This research was supported in part by DARA and the Max-Planck-Institut für extraterrestrische Physik and USRA. D. P. F. is supported under NASA grant NAG 5-1360.

S. L. S. would like to express his appreciation to MPE, J. Trümper, and the entire *ROSAT* group at MPE for the very productive collaboration of the last 10 years. This work would not have been possible without their help and skill.

REFERENCES

Allen, C. W. 1973, Astrophysical Quantities (London: Athlone)
Barber, C. O., Roberts, T. P., & Warwick, R. 1996a, MNRAS, 282, 157
Barber, C. O., Warwick, R., & Snowden, S. L. 1996b, in Röntgenstrahlung from the Universe, ed. H. U. Zimmermann, J. E. Trümper, & H. Yorke (Garching: MPE), 319
Berghöfer, T. W., Lieu, R., Bowyer, S., & Knude, J. 1997, in IAU Colloq. 166, The Local Bubble and Beyond, in press
Berkhuijsen, E. M., Haslam, C. G. T., & Salter, C. T. 1971, A&A, 14, 252
Bertaux, J. L., Lallement, R., Kurt, V. G., & Mironova, E. N. 1985, A&A, 150, 1
Bloch, J. J., Jahoda, K., Juda, M., McCammon, D., Sanders, W. T., & Snowden, S. L. 1986, ApJ, 308, L59
Bochkarev, N. G., & Sitnik, T. G. 1985, Ap&SS, 108, 237
Bowyer, C. S., Field, G. B., & Mack, J. E. 1968, Nature, 217, 32
Bunner, A. N., Coleman, P. L., Kraushaar, W. L., McCammon, D., Palmieri, T. M., Shilepsky, A., & Ulmer, M. 1969, Nature, 223, 1222
Burrows, D. N. 1989, ApJ, 340, 775
Burrows, D. N., & Kraft, R. P. 1993, ApJ, 411, 685
Burrows, D. N., Kraushaar, W. L., McCammon, D., & Sanders, W. T. 1984, ApJ, 287, 208
Burrows, D. N., & Mendenhall, J. A. 1991, Nature, 351, 629
Cox, D. P. 1997, in IAU Colloq. 166, The Local Bubble and Beyond, in press
———. 1981, ApJ, 245, 534
Cox, D. P., & Reynolds, R. J. 1987, ARA&A, 25, 303
Cox, D. P., & Snowden, S. L. 1986, Adv. Space Res., 6, 97
Cui, W., McCammon, D., Sanders, W. T., Snowden, S. L., & Womble, D. S. 1996, ApJ, 468, 102
Dickey, J. M., Salpeter, E. E., & Terzian, Y. 1978, ApJS, 36, 77
Edwards, B. E. 1990, Ph.D. thesis, Univ. of Wisconsin–Madison
Egger, R. 1995, in ASP Conf. Proc. 80, The Physics of the Interstellar Medium and the Intergalactic Medium, ed. A. Ferrara, C. Heiles, C. F. McKee, & P. Shapiro (San Francisco: ASP), 45
ESA 1997. The Hipparcos and Tycho Catalogues (ESA SP-1200) (ESTEC: ESA Publ. Div.)
Ferrière, K. M. 1995, ApJ, 441, 281
Freyberg, M. J., et al. 1998, in preparation
Frisch, P. C. 1995, Space Sci. Rev., 72, 499
Frisch, P. C., & York, D. G. 1983, ApJ, 271, L59
Garmire, G. P., et al. 1992, ApJ, 399, 694
Gry, C., York, D. G., & Vidal-Madjar, A. 1985, ApJ, 296, 593
Guo, Z., & Burrows, D. N. 1997, ApJ, 480, L51
Hartman, D. & Burton, W. B. 1997, Atlas of Galactic Neutral Hydrogen (Cambridge: Cambridge Univ. Press)
Hasinger, G., Burg, R., Giacconi, R., Hartner, G., Schmidt, M., Trümper, J., & Zamorani, G. 1993, A&A, 275, 1
Henry, R. C., Fritz, G., Meekins, J. F., Friedman, H., & Byram, E. T. 1968, ApJ, 153, L11
Herbstmeier, U., Mebold, U., Snowden, S. L., Hartmann, D., Burton, W. B., Moritz, P., Kalberla, P. M. W., & Egger, R. 1995, A&A, 298, 606
Hirth, W., Mebold, U., Dahlem, M., & Müller, P. 1992, Ap&SS, 186, 211
Hobbs, L. M., Blitz, L., & Magnani, L. 1986, ApJ, 306, L109
Jahoda, K., McCammon, D., Dickey, J. M., & Lockman, F. J. 1985, ApJ, 290, 229
Jahoda, K., McCammon, D., & Lockman, F. J. 1986, ApJ, 311, L57
Jakobsen, P., & Kahn, S. M. 1986, ApJ, 309, 682

Juda, M. 1988, Ph.D. thesis, Univ. of Wisconsin–Madison
———. 1996, BAAS, 28(2), 835
Juda, M., Bloch, J. J., Edwards, B. C., McCammon, D., Sanders, W. T., Snowden, S. L., & Zhang, J. 1991, ApJ, 367, 182
Kahn, S. M., & Jakobsen P. 1988, ApJ, 329, 406
Kerp, J. 1994, A&A, 289, 597
Kerp, J., Burton, W. B., Egger, R., Freyberg, M. J., Hartmann, D., & Kalberla, P. M. W. 1997, A&A, submitted
Kerp, J., Herbstmeier, U., & Mebold, U. 1993, A&A, 268, L21
Knapp, G. R. 1975, AJ, 80, 111
Kuntz, K. D., Snowden, S. L., & Verter, F. 1997, ApJS, 484, 245
Kuntz, K. D., Snowden, S. L., & Warwick, R. S. 1998, in preparation
Landini, M., & Monsignori Fossi, B. C. 1990, A&A, 82, 229
Lockman, F. J., McCammon, D., & Jahoda, K. 1986, ApJ, 302, 432
Marshall, F. J., & Clark, G. W. 1984, ApJ, 287, 633
McCammon, D., Burrows, D. N., Sanders, W. T., & Kraushaar, W. L. 1983, ApJ, 269, 107
McCammon, D., & Sanders, W. T. 1990, ARA&A, 28, 657
McKee, C. F., & Ostriker, J. P. 1977, ApJ, 218, 148
Moritz, P., Wennmacher, A., Herbstmeier, U., Mebold, U., Egger, R., & Snowden, S. L. 1998, in preparation
Morrison, R., & McCammon, D. 1983, ApJ, 270, 119
Nousek, J. A., Fried, P. M., Sanders, W. T., & Kraushaar, W. L. 1983, ApJ, 269, 107
Paresce, F. 1984, AJ, 89, 1022
Park, S., Finley, J. P., & Snowden, S. L. 1997, ApJ, 491, 165
Plucinsky, P. P., Snowden, S. L., Aschenbach, B., Egger, R., Edgar, R. J., & McCammon, D. 1996, ApJ, 463, 224
Raymond, J. C. 1992, ApJ, 384, 502
Raymond, J. C., & Smith, B. W. 1977, ApJS, 35, 419
Reynolds, R. J. 1991, in The Interstellar Disk-Halo Connection in Galaxies, ed. H. Bloemen (Dordrecht: Kluwer), 67
Sanders, W. T. 1997, in IAU Colloq. 166, The Local Bubble and Beyond, in press
Sanders, W. T., Edgar, R. J., & Liedahl, D. A. 1996, in Röntgenstrahlung from the Universe, ed. H. U. Zimmermann, J. E. Trümper, & H. Yorke (Garching: MPE), 299
Sanders, W. T., Kraushaar, W. L., Nousek, J. A., & Fried, P. M. 1977, ApJ, 217, L87
Schlegel, D. J., Finkbeiner, D. P., & Davis, M. 1998, in preparation (SFD)
Sidher, S. D., Sumner, T. J., Quenby, J. J., & Gambhir, M. 1996, A&A, 305, 308
Slavin, J. D., & Cox, D. P. 1992, ApJ, 392, 131
Snowden, S. L., Aschenbach, B., Pfeffermann, E., Burrows, D. N., & Sanders, W. T. 1995a, 439, 399
Snowden, S. L., Cox, D. P., McCammon, D., & Sanders, W. T. 1990, ApJ, 354, 211 (SCMS)
Snowden, S. L., et al. 1995b, ApJ, 454, 643
Snowden, S. L., Freyberg, M. J., Schmitt, J. H. M. M., Voges, W., Trümper, J., McCammon, D., Plucinsky, P. P., & Sanders, W. T. 1997, ApJ, 485, 125
Snowden, S. L., Hasinger, G., Jahoda, K., Lockman, F. J., McCammon, D., & Sanders, W. T. 1994a, 430, 601
Snowden, S. L., McCammon, D., Burrows, D. N., & Mendenhall, J. A. 1994b, ApJ, 424, 714
Snowden, S. L., McCammon, D., & Verter, F. 1993, ApJ, 409, L21
Snowden, S. L., Mebold, U., Hirth, W., Herbstmeier, U., & Schmitt, J. H. M. M. 1991, Science, 252, 1529
Snowden, S. L., & Pietsch, W. 1995, ApJ, 452, 627
Snowden, S. L., & Schmitt, J. H. M. M. 1990, Ap&SS, 171, 207
Snowden, S. L., Schmitt, J. H. M. M., & Edwards, B. E. 1990, ApJ, 364, 118
Trümper, J. 1983, Adv. Space Res., 2(4), 241
———. 1992, QJRAS, 33, 165
Voges, W. 1992, in Proc. of Satellite Symp. 3, Space Science with Particular Emphasis on High-Energy Astrophysics, ed. T. D. Guyenne & J. J. Hunt (Noordwijk: ESA), 9
Wakker, B. P., & Boulanger, F. 1986, A&A, 170, 84
Wang, Q. D., & McCray, R. 1993, ApJ, 409, L37
Wang, Q. D., & Yu, K. C. 1995, AJ, 109, 698
Welsh, B. Y., Craig, N., Vedder, P. W., & Vallerga, J. V. 1994, ApJ, 437, 638
Wheelock, S. L. et al. 1994, *IRAS* Sky Survey Atlas Explanatory Supplement (JPL Pub. 94-11) (Pasadena: JPL)